The Gemini-North Multiobject Spectrograph Stability Performance

Richard Murowinski[a], J.R. Allington-Smith[b], S.M. Beard[c], D. Crampton[a], R. Davies[b], C.J. Dickson[c], I.M. Hook[d], I. Jørgensen[e], S. Juneau[a], G.E. Marshall[c], K. Szeto[a], C.J. Tierney[c].

[a]National Research Council of Canada, Herzberg Institute of Astrophysics, 5071 West Saanich Road, Victoria, BC, V9E 2E7, Canada
[b]Department of Physics, Science Laboratories, University of Durham, South Road, Durham, DH1 3LE, U.K.
[c]UK Astronomy Technology Centre, Royal Observatory, Edinburgh, Blackford Hill, Edinburgh, EH9 3HJ, U.K.
[d] Department of Physics, University of Oxford, Nuclear & Astrophysics Laboratory, Keble Road, Oxford OX1 3RH, U.K.
[e]Gemini Observatory, 670 N. A'ohoku Place, Hilo, Hawaii, 96720, USA

ABSTRACT

Of the Gemini Multi-Object Spectrograph's (GMOS) scientific requirements, one which led to technically interesting areas was the ability to measure velocities to a accuracy of 2km/s over the entire 5.5 arcminute square field. GMOS's design to meet this requirement includes a mechanical design for stiffness and without hysteresis or image rotation, and an open loop flexure control system which translates the detector position to compensate for flexure. The model used to predict the flexure is an empirical one developed from measured flexure results. In this paper we present the analysis of factors which enable meeting the 2km/s requirement, and the observing strategies needed to make those observations. We look in particular detail at the development and test of that flexure compensation system, including both lab results and on-telescope results.

Keywords: astronomical instrumentation, spectrograph, flexure

1. INTRODUCTION

The GMOS spectrographs were developed as workhorse facility optical instruments[1–3] for the Gemini telescopes. One of the important objectives set for GMOS was a stability suitable for observation of radial velocities to a accuracy of 2km/s on a single object. This requirement results in the specification of image movement less than $3.125\mu m$/hr (referred to the science detector), independent of wavelength, and expected to be met over the field. Among the options considered in the early stages of design, the concept of an open-loop flexure conpensation system working with a repeatable and stiff instrument structure which has minimal hysteresis won over other closed-loop candidate concepts.

We earlier[4] described design aspects of the instrument directed towards achieving the stability goal. A general description of and recent test results from the instrument can be found elsewhere[5] in these proceedings. In very brief summary here: the prime reference in GMOS for focal plane positional stability and focus to the telescope is the on-instrument wavefront sensor (OIWFS). The spectrograph slit plane is coupled tightly to the OIWFS,[6] and deformation in the spectrograph (i.e. slit to detector flexure) was designed to be repeatable and to be corrected using an open-loop model which positioned the detector translation assembly[7] (DTA) to compensate for flexure-induced image motion. The strategy we adopted to meet the stability requirement was to

Further author information: (Send correspondence to R.G.M.)
R.G.M.: E-mail: Richard.Murowinski@nrc.ca, Telephone: 250 363 0057

1. Ensure both the OIWFS and mask deployment mechanisms were very repeatable and stiff with respect to each other,

2. Ensure the grating/mirror fold movement was repeatable and stable, both when deploying and in tilt,

3. Ensure all optical elements from the mask plane through to and including the detectors were mounted so as to allow a predictable hysteresis-free elastic deformation producing an image translation, but not rotation, as a function of changing gravity vector,

4. Ensure the DTA movement was linear and repeatable,

5. Use the three axes of movement of the DTA to compensate in real time for instrument flexure between the mask plane and detector plane, resulting from thermal changes or a changing gravity vector.

Below, we desrcibe measurements of the major factors which contribute to the error budget for this specification: spectrograph flexure, thermal effects and guiding errors. The results of these tests are summarized at the end.

2. LAB DEVELOPMENT

2.1. Spectrograph Flexure

In the instrument development program, studying dynamic behaviour was scheduled toward the end, followed only by science simulation tests and final acceptance. At this point the instrument was aligned, met static optical requirements, and was fully functional under the control of the instrument control system. Initial dynamic tests included checking the functionality of the instrument at all extreme gravity vectors, and checking that the image movement with changing gravity vector was dominated by elastic deformation (i.e. with little or no hysteresis or non-repeatable movement). During this latter check, we identified a damaged optical mount causing large unpredictable movement, and corrected that before attempting to measure or model flexure characteristics.

2.1.1. Data collection

For studying its flexure behaviour, GMOS was mounted to the large flexure beam at the UK Astronomy Technology Centre (UKATC). The beam is a large welding manipulator capable of supporting GMOS at its mounting face in a manner which mimics telescope mounting, and rotating it about two axes through a series of programmed positions. The range of movement available was large enough to mimic the majority of gravity vector space GMOS would experience at the telescope, but not all of it. During this experiment, a custom optical source unit was mounted on the flexure beam in front of the instrument, capable of providing variable intensity flatfield illumination of GMOS masks as well as providing three artificial stars at fixed positions. The general procedure for most experiments involved using a GMOS focalplane mask containing a number of small pinholes as well as larger apertures for the artificial stars. The instrument was stepped through a program of gravity vectors, and at each sample point images of the pinhole positions or artificial stars were made using the science CCD or the OIWFS's Shack-Hartmann sensor. The flexure beam is not capable of slow sidereal-like movement, so all measurements were taken with the beam stationary between episodes of relatively rapid movement between sample points.

Two coordinate systems were defined for GMOS: the instrument coordinate system, in which X is the slit direction, Y the dispersion direction and Z the focus direction along the optical axis; and the detector coordinate system, in which CCD_x is the serial (horizontal) direction, CCD_y the parallel (vertical) direction and CCD_z the detector focus position. In all cases, the direction of X, Y, CCD_x and CCD_y point toward increasing pixel count. The direction of Z is along the optical path while CCD_z points toward increasing focus stage travel (i.e. toward the telescope, in the opposite direction from Z). For the flexure development, we make use of vectors **X**, **Y** and **Z** which are the vectors of right hand rotation about X, Y and Z, and with an reference of 0 for the case of the instrument mounted on the side port of the cassegrain instrument cube of a zenith-pointing Gemini telescope. The coordinate system is sketched in Figure 1.

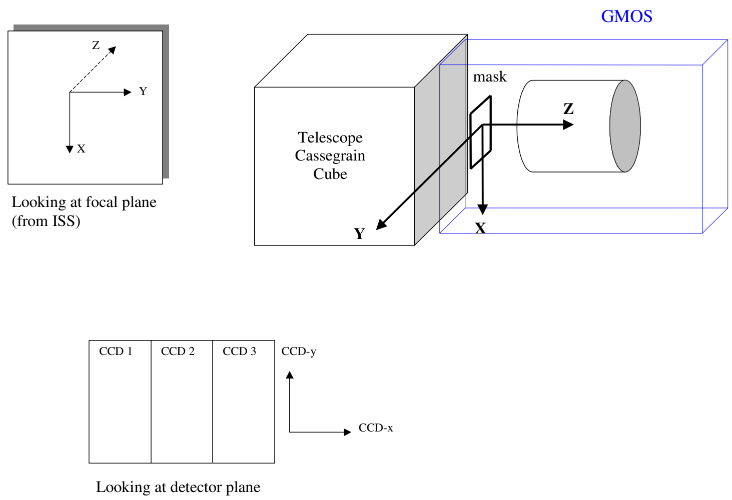

Figure 1. The GMOS instrument coordinate system is seen in the upper two figures and detector coordinate system in the lower figure. Note that the detector coordinates are transposed from the instrument coordinates: instrument X is the same as CCD_y. GMOS is sketched as mounted on one of the side ports of the cassegrain instrument support cube.

2.1.2. Mask to detector flexure

The flexure beam was moved through sweeps of rotation about **Y** while keeping **Z** fixed. The **Z** angle was then changed to a new value and the next sweep carried out etc., until a grid of **Y** and **Z** positions had been covered with approximate spacing 20 degrees. Finally one sweep through **Z** with **Y** fixed was done as a cross check and to tie the data together. At each position an image of the pinhole mask was taken and a Hartmann focus test was performed.

For initial assessment of the flexure, sine curves were fitted to each sweep individually. The amplitudes of these fits were used to estimate the expected displacement over a period of 1 hr (equivalent to 15 degrees of motion). Column (a) of Table 1, found in the summary at the end of this document, gives the results of these uncorrected flexure measurements. We have estimated the maximum displacement per hour for each sweep using two methods - the first is to use the fact that for a sinusoidal function the maximum rate of change per hour is simply $0.26 \times A$ where A is the amplitude. The second method was to take the largest displacement seen between successive positions and scale this by 15/20 to correct for the fact that grid of positions is spaced every 20 degrees rather than 15. This method has the advantage of being a real measurement and hence sensitive to any non-sinusoidal component of the flexure, but has the disadvantage of being more susceptible to noise fluctuations on individual measurements.

2.1.3. Making the flexure model

For each of CCD_x, CCD_y and CCD_z, a surface of displacements was constructed as a function of gravity vector **Y** and **Z**, as shown in Figure 2. The sweeps at constant **Z** all go through the **Y**=-90 degree position, and this point was used as a reference to match the various data sets together. The sweeps at constant **Y** were then matched to the rest of the data at **Z**=0. After constructing the surfaces, a sinusoidal model was fit to the data. A different functional form was used for CCD_x and CCD_y. Focus data confirmed the original design analysis that flexure-induced focus changes are too small to affect performance, and so no model was developed for CCD_z.

The functions used, and their derived coefficients were:

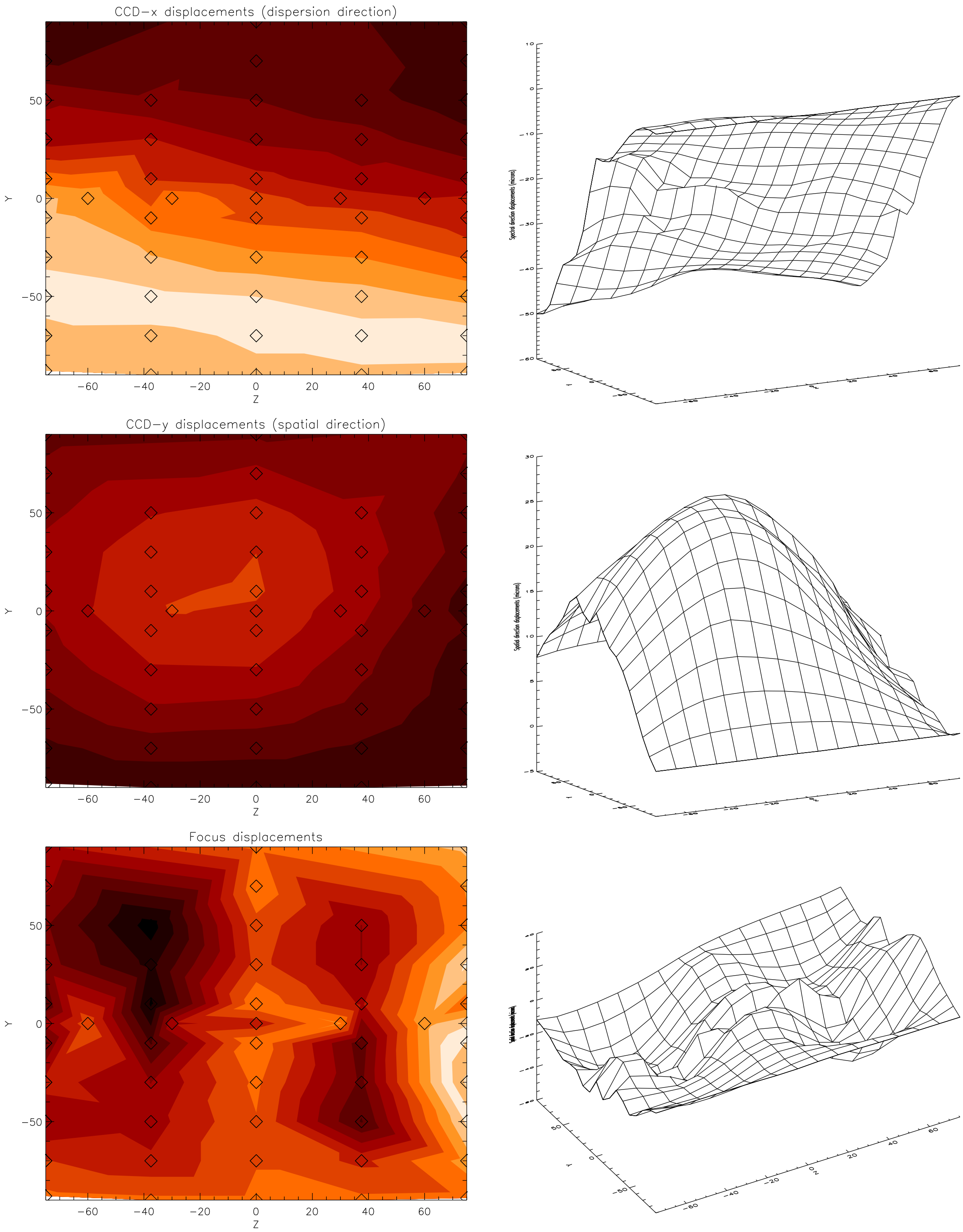

Figure 2. Flexure surfaces for CCD_x, CCD_y, and CCD_z. Fits to these surfaces define the coefficients of the flexure model.

CCD_x

$$dx = a0sin(Y + a1) + a2sin(Z + a3) + a4$$

$$a0 = 23.53, a1 = 179.70, a2 = 5.51, a3 = 165.7, a4 = -25.24$$

CCD_y

$$dy = a0sin(Y + a1)sin(Z + a2) + a3$$

$$a0 = 21.32, a1 = 74.35, a2 = 105.25, a3 = 4.02$$

The data, fit and residuals *from the fit* are shown for the representative CCD_y direction in Figure 3. This model was then incorporated into the instrument control software and the full set of flexure data reobtained. The resulting *measured* residuals for both CCD_x and CCD_y are shown in Figure 4. The expected and measured residuals generally agree very well, indicating that the flexure is repeatable and that the control system is correctly moving the DTA with the output of the above model. Column (b) in Table 1 gives a summary of these results. This shows that the effects of flexure are reduced by a factor of about 4 with the compensation model running.

The model was then tested in a sample space different from that used to derive the model. Two different tests were conducted: a random positioning test and a tracking test. In the random positioning test, the flexure beam was slewed to different random gravity vectors and the image position shift measured at each position. This test maximizes the effect of any non-repeatability or hysteresis in GMOS. In the tracking tests, the flexure beam was moved to simulate the track that a telescope would follow when tracking a star for 5 hrs. Even though the test involved abrupt starts and stops of movement along the sidereal track, the results were nevertheless good. The results of these 'random positions', as well as that for 'example track' are given in Table 1, column (b) in the summary at the end.

2.1.4. Rotation and scale changes

Mask to CCD rotation and scale changes were measured using positions of the 5 spots which were gathered during the course of X, Y and Z displacement measurements. Image rotation was found to be less than 20 $\mu radians$/hour, and scale changes less than 3.5 X 10^{-5}/hour. Both of these, when evaluated as image movement at the edge of the field, are within the amount budgeted.

2.1.5. Flexure during spectroscopy: the Anamorphic factor

In a grating, unlike the case with a plane mirror, the incident and reflected rays do not make the same angle with respect to the grating normal. As a result, the scaling factor of image movement resulting from mechanical flexure could be modified by the grating angle. This anamorphic factor, A, is given by

$$A = \frac{D_2}{D_1} = \frac{cos\beta}{cos\alpha}$$

where α and β are the angles of incident and dispersed light measured from the grating normal. D_1 and D_2 are the sizes of the beam at the collimator and camera respectively, measured in the dispersion direction.

These angles can be calculated from the grating equation $m\rho\lambda = sin\alpha + sin\beta$ where ρ is the grating ruling density, m is the spectral order and λ is the wavelength; with the constraint that the collimator-camera angle, $\Psi = \alpha - \beta$, is fixed [50 deg]. By differentiating the grating equation with respect to the input and output angles we find

$$\left|\frac{d\beta}{d\alpha}\right| = \frac{1}{A}$$

This means that any deviation in the angle of a ray which happens *before* the grating, $d\alpha$, will be transmitted into the camera at a different angle, $d\beta$, where it will result in a displacement on the detector. This happens unless the grating is used in zero order ($m = 0$) in which case it acts like a plane mirror for which $A = 1$.

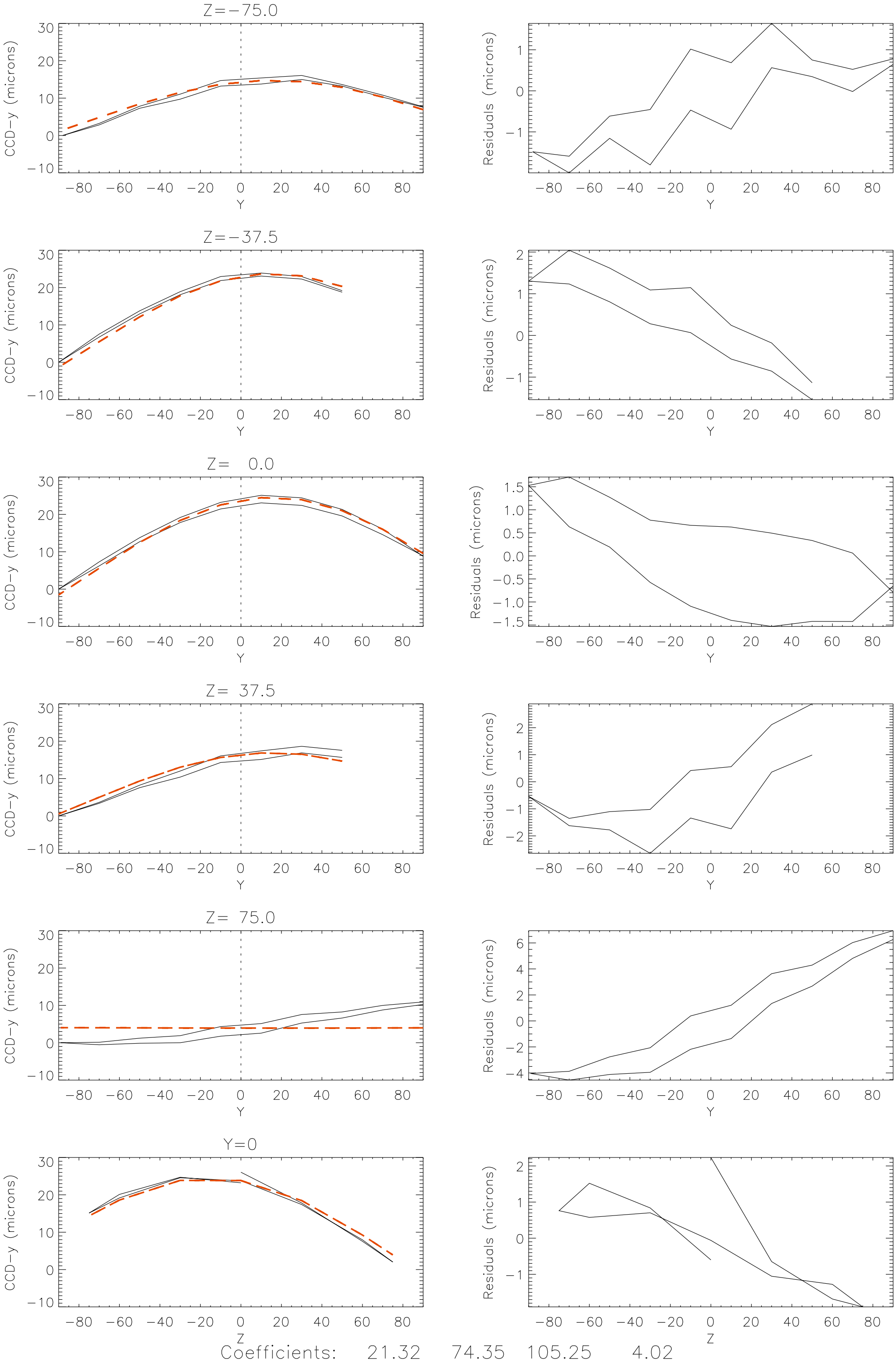

Figure 3. Left pane shows the uncorrected flexure (solid line) and modelled fit to that data (dashed line). In all cases, the measurement swept out a range of angles and then returned over the same course, seen here as two lines of data. The right pane shows residuals to the fit. Data for CCD_y are shown here, although results for CCD_x are similar.

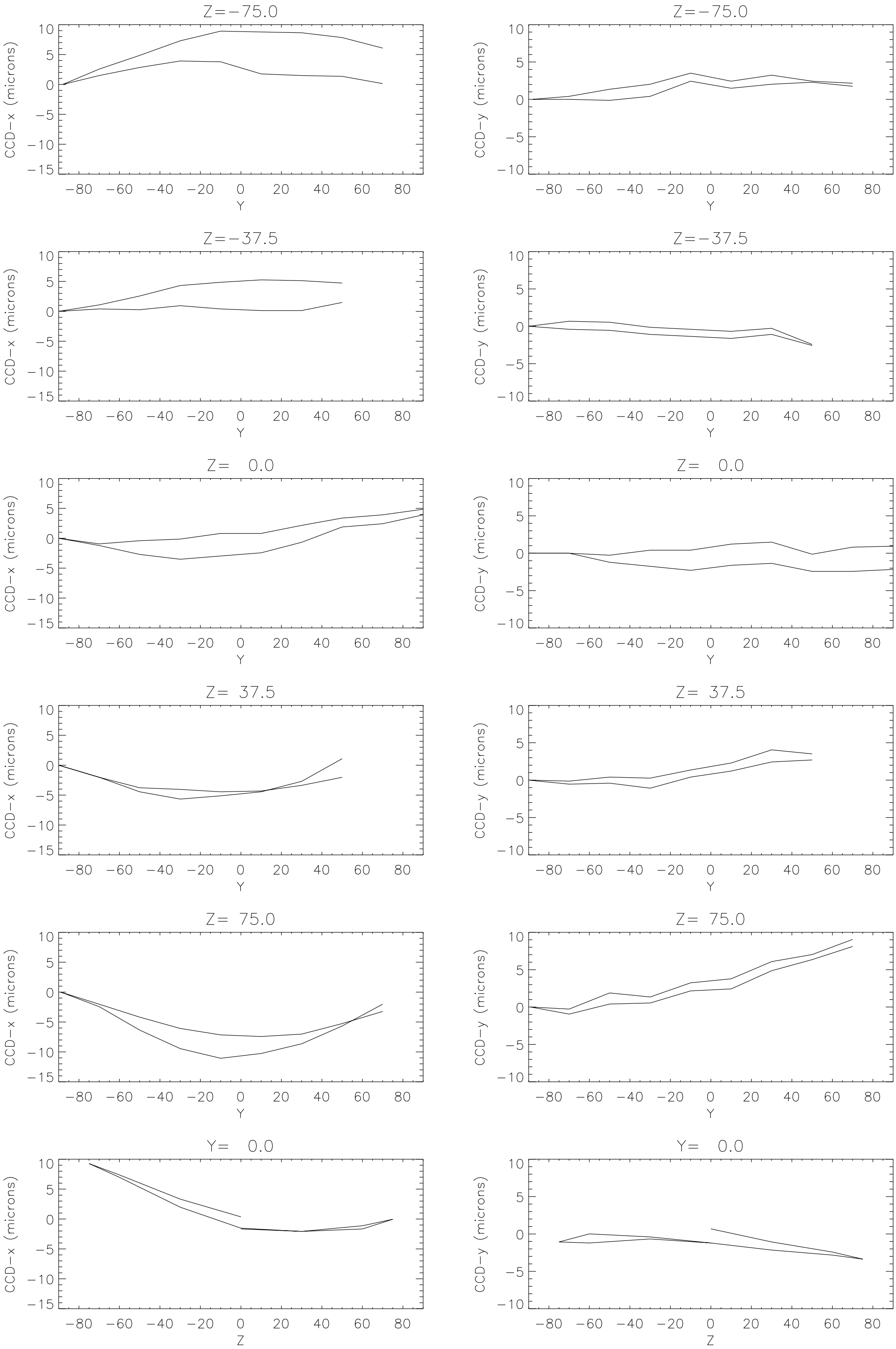

Figure 4. Residuals to lab flexure data, taken by remeasuring the flexure while the correction model was operating in the instrument control system.

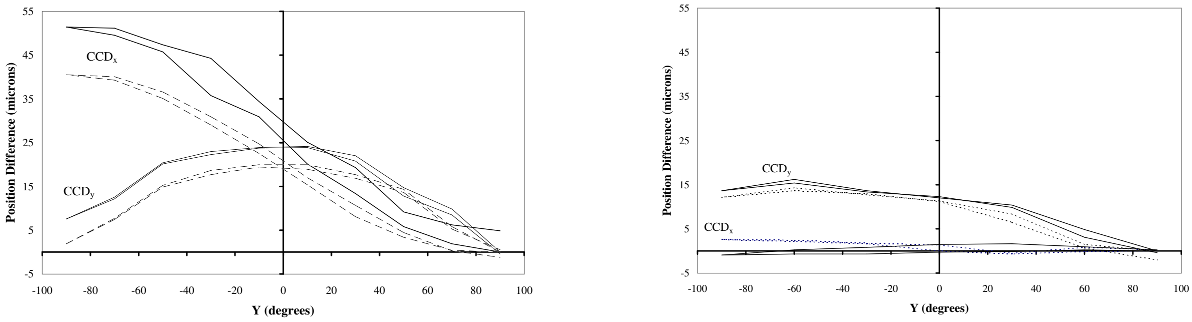

Figure 5. The left pane shows the image displacement for CCD_x and CCD_y, without flexure compensation in place, for the cases of anamorphic factor $A = 1$ (solid lines) and $A = 1.72$ (dashed lines). In the right pane, we see measurements of the same two anamorphic factors, taken with the flexure compensation running and with $H = 0.5$. A clear and similar reduction in flexure for both anamorphic extremes is seen in the dispersion direction CCD_x.

However, any deviation in the angle of a ray occurring *after* the grating will be transmitted through to the camera without modification. Therefore we have the possibility that the flexure should be modelled in two parts: that which occurs before the grating and which will therefore be modified by the anamorphic factor, and the part which occurs after the grating and is therefore not affected. This only relates to the dispersion direction: there is no anamorphism in the spatial direction.

To estimate this effect, we carried out flexure tests in the same manner as previously, but with the R831 grating in zero order ($A = 1$), as well as dispersed to give $A = 1.72$. In normal use, $A \leq 1.4$, so this is a very extreme anamorphic factor. In each case, we recorded the position of the image of a pinhole in the same mask as used previously. The results are shown in the left pane of Figure 5 for CCD_x and CCD_y, where the solid lines are $A = 1$ data and dashed lines $A = 1.72$. All flexure correction was turned off.

It can be seen that there is a systematic difference in the dispersion direction which might be due to this effect. However the signal/noise of the detection of this effect is low since the overall amount of flexure is small and because of the non-repeatable component of flexure which appears here as a noise source. This explanation is supported by the difference in CCD_y values between runs which cannot be due to anamorphism!

It was decided to implement a simple correction to the flexure correction calculated from data obtained with the imaging mirror (Section 2.1.2) which could be adjusted via a single parameter as desired. This takes the form of a multiplicative factor applied in the dispersion direction only (CCD_x):

$$g = 1 - H(1 - \frac{1}{A})$$

.

Parameter H is set by the user. Full correction is applied when $g = 1$ which occurs when $H = 0$ or $A = 1$, as required. From the above data, we estimate that $H = 0.5$ and have implemented that as a default value in the GMOS software. The veracity of this model (with the default H value) was checked by sweeping through a range of $\mathbf{Y}$ (with $\mathbf{Z} = 0$), again with both values of A. The results are shown in the right pane of Figure 5.

2.2. Thermal Behaviour

There are two significant contributors to image instability in GMOS as a result of temperature changes: image movement and plate scale change. The first of these, image movement was extensively monitored during the instrument cold tests. During these tests, the entire instrument was installed in a thermal chamber and cycled

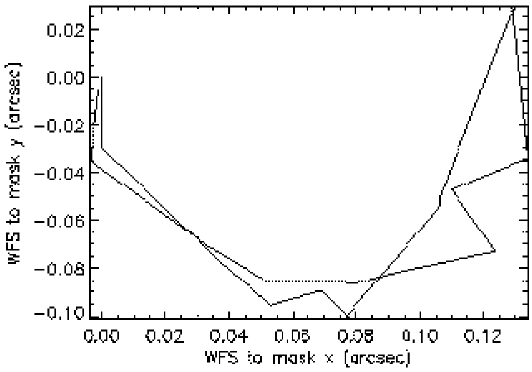

Figure 6. Position difference of an artificial star seen by the GMOS OIWFS compared with that star's position on the mask plane, as the instrument is tipped through 160 degrees and then back again.

slowly in temperature over the operating range of -5C to +5C, while imaging a pinhole mask and taking Hartmann focus measurements. For data taken when the rate of temperature change was slow and comparable to that which it might experience at Mauna Kea, we found that the CCD_x position varied +2.03μm/C, CCD_y by -3.06μm/C and CCD_z by 22μm/C. The typical temperature slew rates which the insulated GMOS is expected to experience during the Mauna Kea nighttime is 0.3C/hr, for which we see the image movement in CCD_x is +0.61μm/hr, CCD_y is -0.91μm/hr and 6.6 μm/hr in the CCD_z direction. Plate scale changes were not measured directly, but modelled by Zemax during design to be 0.48 μm/hr at the edge of the field. All of the thermal effects met spec for use in the Gemini-North thermal environment.

2.3. Guiding Errors

A third area of concern in meeting the accuracy requirement was that of guiding errors, which might be introduced if the OIWFS frame of reference experienced significant flexure with respect to the mask. To explore this area, we monitored the position reported by the OIWFS sensor looking at an artificial star, while alternately imaging that artificial star with the science CCD through a larger hole in the focal plane mask to determine that star's position in the mask plane. The difference between these two is then the relative OIWFS to mask movement. The motion was converted to arcseconds on the sky, in the instrument coordinate system. For the case of mask to CCD flexure this is a straightforward scaling, and flipping of the CCD_y coordinate. In the case of the OIWFS this is more complicated because the OIWFS detector has a different relative rotation from the instrument coordinate system when the OIWFS probe looks at different parts of GMOS's field. The transformation between OIWFS CCD coordinates and mask coordinates for the field location of the artificial star was measured by moving the OIWFS probe through known positions and recording the position of the image on the OIWFS detector.

Figure 6 shows the results of one representative data set: the difference between the position of the artificial star referred to the mask and referred to the OIWFS sensor, as the instrument is tipped through 160 degrees in 20 degree steps, and then back again. Note that the movement is elastic and repeatable. The results of these tests, found in the summary at the end, in the 'lab' column of Table 2, indicate that we would meet our requirement without using a pointing model to correct for this flexure. The addition of a pointing model is possible at a later time if the need for improved performance merits it.

3. TELESCOPE RESULTS

After shipping GMOS, the mask to CCD flexure was then re-measured with GMOS on the Gemini-North telescope, with the same flexure compensation model running as had been derived in the lab. To do this the cassegrain rotator was fixed at various positions and the telescope moved in altitude to the following positions:+90, +60, +30, +17 and then the same in reverse. Images of the pinhole mask, illuminated with the telescope's internal calibration unit were taken at each position and the displacements in CCD_x and CCD_y were recorded. The results are summarised in column (c) of Table 1. This shows that the effects of flexure are significantly reduced (by a factor of about 2) compared to the uncorrected flexure measured in the lab, but also that the compensation is not as effective as it could be. A candidate explanation for this difference is that the stiffness of the cassegrain mounting cube on the telescope is different from the mounting face on the flexure beam at UKATC. Since that surface is effectively a structural component in GMOS's truss structure, changes to it would influence how GMOS flexes. To get the best results from the flexure compensation system it will be necessary to revise the model using data taken with the instrument mounted on the telescope. The performance found using the lab-derived model was found to be acceptable for instrument modes commissioned to date, but may not be acceptable for the precision radial velocity mode to be commissioned upon the arrival of the atmospheric dispersion corrector, scheduled for early 2003.

The mask-to-detector flexure was also measured while tracking a star on the sky for about 1.5hrs. The inferred flexure per hour is given in Table 1 column (d). The displacements seen are consistent with the range of those shown in column (c).

Finally, the relative flexure between the OIWFS and the GMOS mask plane was measured by imaging a star through a large hole in a GMOS mask while guiding with the OIWFS. The mask also had several pinholes which allowed the mask-to-detector flexure to be monitored so that this could be subtracted from the star-to-detector flexure. The test ran for approximately 1.5hrs as the telescope crossed the meridian.

The test showed OIWFS-to-mask flexure of 0.022 arcseconds/hour in X and 0.0036 arcseconds/hr in Y (both measured at the science CCD). This compares favorably with results obtained from a similar test while guiding with one of the facility wavefront sensors, located much further away, which showed relative flexure of approximately 0.1 arcseconds/hr with respect to GMOS.

4. SUMMARY

Table 1: Summary of mask to detector flexure results.

	(a) lab no model	(b) lab with model	(c) Gemini-N with model	(d) Gemini-N (sky) with model
Mask to CCD_x displacement ($\mu m/hr$)				
Mean	3.7	1.0	1.7	
Peak expected of sinusoidal function	6.8	2.5	5.3	
Peak measured	7.2	2.9	9.8*	
Example track		0.6		1.0
Random positions (μm rms)		3.0		
Mask to CCD_y displacement ($\mu m/hr$)				
Mean	2.5	0.4	0.6	
Peak expected of sinusoidal function	5.8	1.2	2.2	
Peak measured	5.9	1.8	2.0	
Example track		0.5		1.8
Random positions (μm rms)		1.6		

Tables 1 and 2 give a summary of the measured components of spectrograph and OIWFS-mask flexure. The contributions to image movement, as measured in the lab before shipping the instrument to the telescope, was made up of:

Table 2: Summary of WFS-to-mask flexure results.

	lab	Gemini-N (sky)
OIWFS to mask X displacement (mas/hr)		
Mean	11	
Peak expected from sinusoidal function	23	
Peak measured	46*	
Example track	3.2	22
Random positions (mas rms)	43	
OIWFS to mask Y displacement (mas/hr)		
Mean	22	
Peak expected from sinusoidal function	48	
Peak measured	77*	
Example track	13.2	3.6
Random positions (mas rms)	33	

* = maximum displacement between successive points is large due to noise or non-sinusoidal variation

- Spectrograph flexure, which is made up of 1.45μm/hr at the edge of the field for plate scale changes, 0.62μm/hr for image rotation, and 0.96μm/hr of mean CCD_x image movement when using flexure compensation. The RSS combination of these is 1.85μm/hr.
- Thermal effects, which is made up of 0.61μm/hr of temperature-induced image motion and 0.48μm/hr image movement at edge of field due to plate scale change, for an RSS combination of 0.78μm/hr.
- Guiding errors, for which we use an average of the X and Y values during tracking tests: 0.0065 arcseconds/hr or 1.22μm/hr at the science detector.

The RSS combination of these three error sources is 2.35μm/hr, which compares favourably with the 3.125μm/hr specification derived from the science requirements.

With measurement made with the instrument on the telescope (but still using the lab flexure model), we have information to revise some of these numbers. Replacing the spectrograph flexure mean CCD_x image movement with the telescope-measured value of 1.7μm/hr, and also replacing the guiding error with the average X and Y values during telescope tracking tests: .0128 arcseconds/hr (2.4μm/hr at the science CCD), the RSS combination of the same factors as before is now 3.43μm/hr.

We believe that GMOS, even with the lab model in use at the telescope, is the most stable cassegrain mulit-object spectrograph ever built for a large telescope. That stability enables extremely accurate velocities to be obtained in multi-slit mode (as well as facilitating data reduction, flat fielding, object acquisition, etc.). This excellent stability performance can be enhanced further by revising the flexure compensation model for telescope conditions, as well as adding a model to correct differential flexure between the OIWFS and mask.

REFERENCES

1. R.L. Davies, *et. al.* " GMOS: The GEMINI Multiple Object Spectrographs" in *Optical Telescopes of Today and Tomorrow: Following in the Direction of Tycho Brahe*, Arne Ardeberg, ed., *Proc. SPIE* **2871**, pp. 1099–1106, 1996.
2. D. Crampton, *et. al.* "Gemini multi-object spectrograph GMOS: integration and tests" in *SPIE Conference on Optical and IR Telescope Instrumentation and Detectors*, Masanori Iye and Alan F. Moorwood, eds., *Proc. SPIE* **4008** pp. 114–122, 2000.

3. R. Murowinski, *et. al.* "The GEMINI Multiobject Spectrographs" in *SPIE Conference on Optical Astronomical Instrumentation*, Sandro D'Odorico, ed., *Proc. SPIE* **3355**, pp. 188–195, 1998
4. K. Szeto, R. Murowinski, S. Roberts, L. Saddlemyer, R. Bennett, C. Dickson, R. Hastings, "Gemini Multi-Object Spectrograph - A Flexure Critical Design", in *SPIE Conference on Optical Astronomical Instrumentation*, Sandro D'Odorico, ed., *Proc. SPIE* **3355**, pp. 297–306, 1998.
5. I. Hook, *et. al.* "The Gemini-North Multiobject Spectrograph Integration, Test and Commissioning", this conference, *Proc. SPIE* **4841-**185, 2002.
6. S. Roberts, M. Fletcher, B. Leckie, L. Saddlemyer, K. Szeto, J. Sebesta, "Opto-Mechanical Design of the Gemini Multi-Object Spectrograph On-Instrument Wavefront Sensor", in in *Optomechanical Design and Precision Instruments*, Alson E. Hatheway, ed., *Proc SPIE* **3132**, pp. 184–195, 1997.
7. P.R. Hastings, "Focus and translation mechanism for the Gemini Multi-Object Spectrograph (GMOS)" in *Optical Telescopes of Today and Tomorrow: Following in the Direction of Tycho Brahe*, Arne Ardeberg, ed., *Proc. SPIE* **2871**, pp. 1216–1221.